MATERIALS SCIENCE

2017 © The Authors, some rights reserved; exclusive licensee American Association for the Advancement of Science. Distributed under a Creative Commons Attribution NonCommercial License 4.0 (CC BY-NC).

Assembly of mesoscale helices with near-unity enantiomeric excess and light-matter interactions for chiral semiconductors

Wenchun Feng,[1] Ji-Young Kim,[2] Xinzhi Wang,[1]* Heather A. Calcaterra,[1] Zhibei Qu,[1] Louisa Meshi,[3] Nicholas A. Kotov[1,2†]

Semiconductors with chiral geometries at the nanoscale and mesoscale provide a rich materials platform for polarization optics, photocatalysis, and biomimetics. Unlike metallic and organic optical materials, the relationship between the geometry of chiral semiconductors and their chiroptical properties remains, however, vague. Homochiral ensembles of semiconductor helices with defined geometries open the road to understanding complex relationships between geometrical parameters and chiroptical properties of semiconductor materials. We show that semiconductor helices can be prepared with an absolute yield of *ca* 0.1% and an enantiomeric excess (e.e.) of 98% or above from cysteine-stabilized cadmium telluride nanoparticles (CdTe NPs) dispersed in methanol. This high e.e. for a spontaneously occurring chemical process is attributed to chiral self-sorting based on the thermodynamic preference of NPs to assemble with those of the same handedness. The dispersions of homochiral self-assembled helices display broadband visible and near-infrared (Vis-NIR) polarization rotation with anisotropy (*g*) factors approaching 0.01. Calculated circular dichroism (CD) spectra accurately reproduced experimental CD spectra and gave experimentally validated spectral predictions for different geometrical parameters enabling *de novo* design of chiroptical semiconductor materials. Unlike metallic, ceramic, and polymeric helices that serve predominantly as scatterers, chiroptical properties of semiconductor helices have nearly equal contribution of light absorption and scattering, which is essential for device-oriented, field-driven light modulation. Deconstruction of a helix into a series of nanorods provides a simple model for the light-matter interaction and chiroptical activity of helices. This study creates a framework for further development of polarization-based optics toward biomedical applications, telecommunications, and hyperspectral imaging.

INTRODUCTION

The molecular and nanoscale chirality of biomolecules, surfactants, and liquid crystals, as well as hybrid materials constructed thereof, have been extensively studied and are generally well understood (*1*–*3*). The strong dichroic response of individual plasmonic nanoparticles (NPs) and their assemblies guided by antibody-antigen pairing (*4*), DNA bridges (*5*), or liquid crystals (*6*) has resulted in a rapid increase of research on chiral inorganic nanoscale structures over the past decade (*4*, *7*–*11*). High polarizability of metals, combined with asymmetric geometries with characteristic lengths of 10 to 1000 nm, led to markedly strong chiroptical activity with previously unknown chiral anisotropy (*g*) factors (*4*, *5*, *8*–*18*). Utilization of these constructs in environmental analysis (*4*), DNA biomarker detection (*5*), chiral detection (*10*), and chiral catalysis (*19*) followed.

Although significant progress has been made toward understanding the relationship between the optical activity and geometrical parameters of plasmonic nanostructures (*4*, *5*, *10*, *12*, *18*, *20*–*23*), nanoceramics (*24*, *25*), and nanocarbons (*26*–*28*), knowledge about these relationships for commonly used semiconductor nanomaterials remains cursory (*15*, *29*–*32*). Versatility of synthetic methods and chemical, physical, and biological properties of chiral semiconductor nanomaterials (*9*, *15*, *33*) make them attractive candidates for polarization-based optical devices, catalysts, and biomedical imaging. Here, we intend to advance current understanding of the geometry-property relationship of chiral semiconductor nanomaterials, knowledge that will guide the materials design of inorganic nanostructures with application-adapted chiroptical properties.

Chiroptically active semiconductor nanomaterials can be made using self-assembly processes that are sensitive to subtle anisotropies in interparticle forces (*34*). With background knowledge in the preparation of cysteine-stabilized CdTe NPs and their agglomeration behavior (*32*, *35*), we report that self-assembly of L-cysteine (L-Cys)– or D-cysteine (D-Cys)–stabilized CdTe NPs yields mesoscale helices of single-handedness. This handedness depended solely on the specific Cys enantiomer: D-Cys CdTe NPs assembled into right-handed helices (R-helices), whereas L-Cys CdTe NPs afforded left-handed helices (L-helices). Considering that even for supramolecular structures made from perfectly monodispersed constitutive units, the homochiral yield of produced structures is not a given outcome and requires careful optimization of assembly conditions (*36*–*38*), this ability of NPs made with certain size dispersity is quite remarkable. Furthermore, these mesoscale semiconductor helices present an opportunity to establish the relationships between the geometry and chiroptical activity of semiconductors. Previous methods of preparation of nanoscale, mesoscale, and microscale helicoids from various semiconducting materials, that is, ZnO (*39*), ZnS (*40*), InP (*41*), InGaAs/GaAs (*42*), and CdS (*43*), yielded racemic mixtures that did not display chiroptical activity, with the exception of MoS_2 nanofibers formed under stirring (*33*) and CdTe/CdS twisted ribbons formed under illumination of circularly polarized light (CPL) (*15*).

The CdTe helices prepared here displayed broadband visible and near-infrared (Vis-NIR) rotatory activity with anisotropy (*g*) factor approaching 0.01. An experimentally validated computational model helped in understanding the complex relationship between geometry and optical activity. A simplified heuristic model complements the computational

[1]Department of Chemical Engineering, University of Michigan, Ann Arbor, MI 48109, USA. [2]Department of Materials Science and Engineering, University of Michigan, Ann Arbor, MI 48109, USA. [3]Department of Materials Engineering, Ben-Gurion University of the Negev, Beer-Sheva, Israel.
*Present address: School of Energy Science and Engineering, Harbin Institute of Technology, Harbin, China.
†Corresponding author. Email: kotov@umich.edu

toolbox. Both models enable comparison with other material classes, that is, metals, ceramics, and plastics, with helicity in the same scale that systematically presented their relative advantages or disadvantages and paved the way for predictive design of chiral inorganic nanostructures for telecommunications (*44*), deep tissue imaging (*45*, *46*), and remote sensing (*47*).

RESULTS

Self-assembly of helices

Assembly patterns of CdTe NPs are dependent on the interplay of multiple forces. Because of reduced ionization of the carboxyl and amino groups, the attractive forces between polar NPs become stronger than repulsive electrostatic ones when the medium around NPs changes from water to methanol, enabling self-assembly with chiral asymmetry influenced by short-range interactions. Although most of the NPs in the dispersion produce stochastic aggregates (absolute yield of helices is *ca* 0.1%, section S1), a subset of Cys-stabilized CdTe NPs in methanol undergo self-assembly, forming well-defined helices. Evaluated with scanning transmission electron microscopy (STEM) tomography (Fig. 1, A and B, and movies S1 and S2), the helices combine nanoscale, mesoscale, and microscale features: The thickness of their "wings" is below 100 nm, their diameter is ~300 nm, and their length is ~2 μm. The shape of the assembled structure is a helicoid instead of a spiral, with no intrahelical racemization.

Unlike other known processes of enantioselective synthesis yielding products of modest e.e., often in single percent range (*15*, *35*, *48*, *49*), this multiparticle assembly process results in near-unity e.e. with respect to the helices. The handedness of as-formed semiconductor helices is defined by surface ligand: L-Cys leads to homochiral helices with left-handed geometry, whereas D-Cys leads to homochiral helices with right-handed geometry (Fig. 1, C and D). When an achiral stabilizer such as thioglycolic acid (TGA) was used as the stabilizer for CdTe NP synthesis, assemblies formed under identical experimental conditions appeared to have no observable helicity (fig. S1).

A statistically significant number of helices (>100) was surveyed by SEM in random regions of a drop-cast sample to determine e.e. for L- and D-Cys CdTe assemblies. The e.e. approaches 100% for both: L-Cys CdTe NPs assembled into 100 L-helices and one R-helix (e.e., 98%); D-Cys CdTe NPs produced 101 R-helices and no L-helix (e.e., 100%). The rare helix with "abnormal" handedness (for example, the R-helix formed within L-Cys CdTe assemblies) has a distinctly different morphology of the wings (fig. S2). Stochastic aggregates did not reveal any preferred handedness at the scale characteristic of SEM images.

Our helices contain a nanowire core (Fig. 1E) that is twisted into the same direction as the wings and has a diameter of ~60 nm (Fig. 1F). Attached to the nanowire core are crystalline grains (Fig. 1G, 1H). Selected-area electron diffraction (SAED) (Fig. 1I) shows ring patterns that can be indexed to CdS [Joint Committee on Powder Diffraction Standards (JCPDS) card no. 75-0581] and CdTe (JCPDS card no. 19-0193). The nanowire core shows lattice spacing of 0.40 and 0.59 nm (Fig. 1J), which correspond to the (100) and (001) planes of hexagonal tellurium (Te; JCPDS card no. 36-1452). Fast Fourier transform (FFT) of electron diffraction (inset, Fig. 1J) displayed reflexes matching the (001), (100), and (101) facets of the Te single crystal. Elemental mapping using STEM with in situ energy-dispersive x-ray (EDX) spectroscopy indicates that O, S, Cd, and Te elements are present throughout the helix (Fig. 1, K to R). As expected, there is an excess of Te (Fig. 1R) within the nanowire core compared to the rest of the helix. We attribute the presence of single-crystalline Te to the previously reported (*50*, *51*) oxidation of Te^{2-} ions from CdTe.

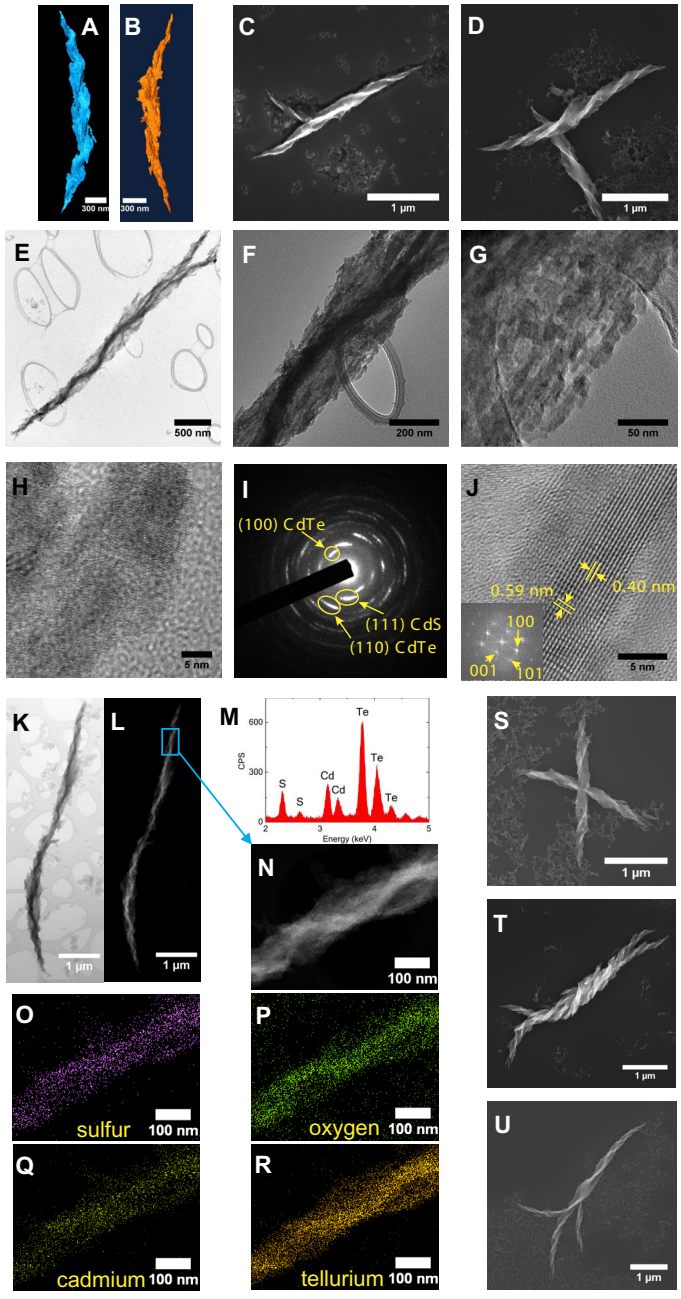

Fig. 1. Structural and elemental analysis of mesoscale helices. STEM tomography of (**A**) R-helix and (**B**) L-helix. Scanning electron microscopy (SEM) images of (**C**) R-helix assembled from D-Cys CdTe NPs and (**D**) L-helix assembled from L-Cys CdTe NPs. TEM images of an R-helix at (**E**) low, (**F**) medium, and (**G**) high magnification. (**H**) High-resolution TEM (HRTEM) of helix boundary. (**I**) SAED graph. (**J**) HRTEM of nanowire core (inset, FFT graph). (**K**) Bright-field STEM and (**L**) High-angle annular dark-field imaging-STEM (HAADF-STEM) imaging of R-helix. (**M**) STEM-EDX spectrum. CPS, counts per second. (**N**) HAADF-STEM image of the highlighted region from (L). (**O** to **R**) Elemental mapping of sulfur, oxygen, cadmium, and tellurium, respectively. SEM images of hierarchical assemblies of (**S**) intercrossed helices, (**T**) intertwined helices, and (**U**) dendritic twists.

Formation mechanism

Previous studies indicated that vortex-like force fields at the particle interface that are associated with chiral surface ligands (*35*) and chiral shapes of the NPs are likely to be responsible for helicity of NP superstructures (*15*),

which is consistent with the body of knowledge in the field of helical supramolecular chiral fibers and helical proteins or peptides (*36*). However, a different insight into the assembly mechanism is required to explain the near-unity e.e. that must include detailed knowledge about the stages of assembly process and thermodynamics of NP interactions. Te core consistently displayed a distinct twist (Fig. 1, E, K, and L); therefore, the first question that arises is whether the twisting of the core or the preferentially left or right twist for particle attachment to each other is responsible for the formation of the helices.

To answer this question, we performed TEM analysis during the intermediate steps of helix formation. At the starting point, random aggregates with no specific geometrical shape were observed (Fig. 2A). At 1 hour, a short, thin nanowire (that is, 265 nm long and 14 nm wide) with some attached NPs emerged (Fig. 2B). Lattice fringes of 0.40 and 0.59 nm (Fig. 2C) indicated that the assembly of the helix actually started with the formation of the Te nanowire; no twist in the nanowire was observed at this time. At 3 hours, the Te nanowire grew longer and wider (that is, 656 nm long and 23 nm wide) and a slight bend started developing (Fig. 2D). At 5 hours, the trend continued and the Te nanowire became 1846 nm long and 30 nm wide for the specific helix (Fig. 2E); the bend and tapering at the ends of the superstructure also became pronounced. At 6 hours, fully formed helices emerged; the Te core (that is, 3550 nm long and 61 nm wide) in them acquired a prominent twist (Fig. 2F). After this, the growth slowed down considerably; the Te nanowire at the 8-hour time point was slightly longer (that is, 4071 nm) and thicker (that is, 62 nm; Fig. 2G) than that at the previous checkpoint. This data set indicated that twisting of the core is the secondary process occurring in response to the NP attachment around it.

To further elucidate the assembly mechanism, we prepared two types of racemic dispersions of CdTe NPs. DL-cysteine was used as the ligand for NP synthesis ("racemic by synthesis") for the first one. The second type of racemic dispersion was made by mixing premade dispersions of D- and L-Cys CdTe NPs in a volume ratio of 1:1 ("racemic by mixing"). One might expect that their assembly should lead to achiral structures exemplified by straight ribbons in TGA-CdTe assemblies (fig. S1). In both types of racemic dispersion, the assembled structures unexpectedly contained both left- and right-handed helices (Fig. 2, J to K, and table S1), which canceled out each other's chiroptical activity (fig. S3). There were no straight ribbons. This points to chiral self-sorting of NPs, which apparently recognize and specifically assemble with NPs of the same chirality but not with their mirror images (*52*). The absence of intrahelical racemization in any of these NP compositions, for example, starts left-handed and then changes to right-handed, indicates a strong preference toward homochirality even in the presence of a competing enantiomer. Similar chiral self-sorting has also been observed for fibrous protein hydrogels (*53*) and supramolecular chiral columns (*54*).

Although chiral interactions are generally considered to be weak, the collective behavior of NPs apparently amplifies the effect of seemingly small energetic perturbations to the potential of mean force (*34*). To understand whether the energy of these interactions is sufficient for guiding the assembly of polydisperse building blocks such as NPs, we used isothermal titration calorimetry (ITC) to elucidate enthalpic and entropic effects for NP interactions for pairwise mixing of their enantiomers (fig. S4). The association between NPs of the same handedness, that is, D-to-D and L-to-L titrations, was found to have more negative ΔG than D-to-L titrations, namely D-to-D, -57 kJ mol^{-1}; L-to-L, -46 kJ mol^{-1}; D-to-L, -29 kJ mol^{-1}. Therefore, NPs of the same chirality

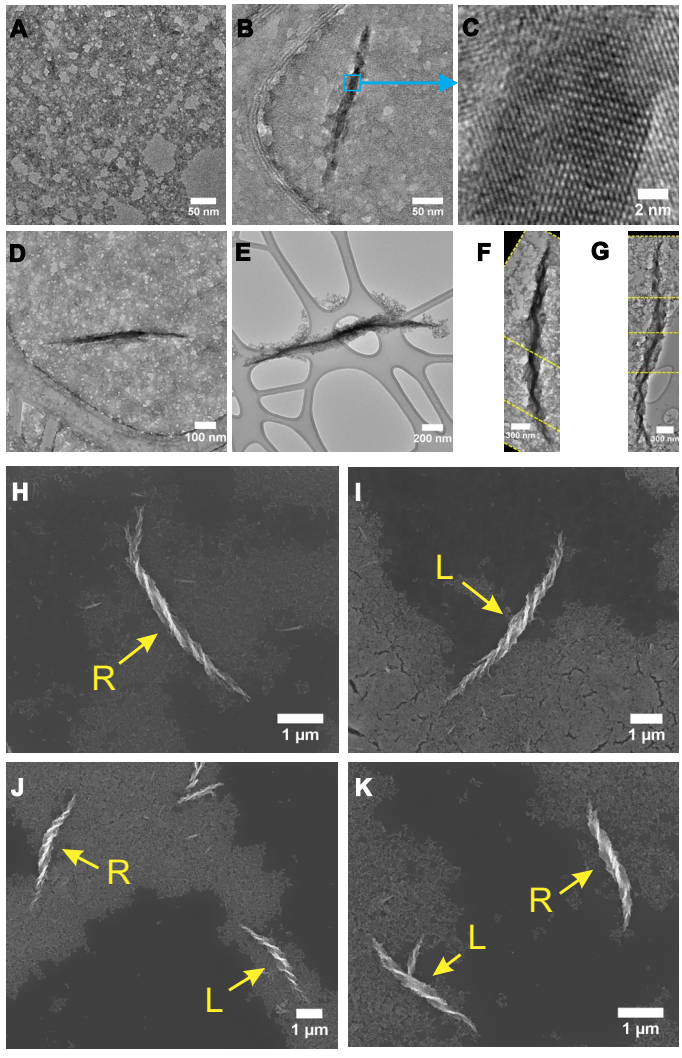

Fig. 2. Formation mechanism. TEM images: self-assembly of D-Cys CdTe NPs at (**A**) 0 hour, (**B**) 1 hour, (**C**) 1 hour at higher magnification of the Te wire, (**D**) 3 hours, (**E**) 5 hours, (**F**) 6 hours, and (**G**) 8 hours. The yellow dashed lines in (F) and (G) represent the edges of the images that were assembled together to display the entire helix. SEM images: (**H**) D-Cys CdTe NP assembly, (**I**) L-Cys CdTe NP assembly, (**J**) DL-Cys CdTe NP assembly, and (**K**) D-Cys CdTe/L-Cys CdTe NP assembly. The arrows point to the helices with designated handedness (L, left-handed helix; R, right-handed helix).

are attracted to each other more strongly than those with opposing chirality, which results in self-sorting and unusually high e.e. values. Note that these thermodynamic data were obtained for the entire ensemble of NPs from which only a small subset proceeds to fully assemble into helices. For this small subset of NPs, the thermodynamic effects of chirality are likely to be even higher.

The helical shape of the assembled structures appears to be similar to the nanofibers spontaneously formed from peptides (*55*, *56*), protein units in the capsids of tobacco mosaic virus (*57*), or chiral macromolecules (*58*). These superstructures represent extended self-organized systems, whereas the helices in Fig. 1 have distinct terminal character, that is, the length and diameter of the helices appear to be restricted. The self-limitation of the growth of helices is likely to be associated with inorganic NPs undergoing oriented attachment (*59*), as can be seen in the formation of polycrystalline

grains in Fig. 1G. The twisting of the Te nanowire core is attributed to the mechanical strain generated during the lattice-to-lattice merger of NPs that bends the entire structure. The rising level of elastic energy and the increase of electrostatic repulsion caused by higher surface charge density should lead to the self-termination.

Chiroptical properties

The helices exhibited characteristic bisignate circular dichroism (CD) spectra with D- and L-Cys CdTe assemblies displaying mirror-image CD bands (Fig. 3A). The assemblies retained their rotatory power after 1 month of storage in the dark at 4°C (figs. S5 and S6). Coexisting random aggregates, with no observable chiral arrangements, were found to contribute only marginally to the overall rotatory power (fig. S7).

CdTe assemblies showed broadband Vis-NIR rotatory activity from 350 to 1800 nm (inset, Fig. 3A, and fig. S8). This specific polarization-active wavelength range may offer unique opportunities in biomedical applications (biological optical window, 650 to 1350 nm).

Individual CdTe NPs generally have weak chiroptical activity and low *g* factor values on the order of 10^{-5} (fig. S9). Upon assembling into CdTe helices, the *g* factor for both L- and R-helices reached ~0.01 at λ = 900 nm (Fig. 3B), which is more than two orders of magnitude higher than that of the NPs and a significant improvement over previously reported chiral CdTe nanostructures (*15*, *35*). The *g* factor value is comparable to those reported for chiral nanoscale assemblies based on metallic components such as Au/Ag pyramids (*8*) and Au helices (*10*), as well as helical organic polymers including protein secondary structures (*60*) and polyacetylene derivatives (*61*).

Geometry- and materials-driven chiroptical response

To understand the relationship between the helix geometry, constituent material(s), and the helix chiroptical properties, we carried out simulations to examine the influence of each geometrical parameter on chiroptical activity. A finite-difference time-domain (FDTD) Maxwell solver was used to analyze the interaction of circularly polarized photons with model structures using wavelength scale features.

The five geometrical parameters of interest include handedness, pitch, length, diameter, and thickness (Fig. 4A). Their effect on CD and *g* factor spectra as quasi-independent variables was investigated. Addition of the Te nanowire core within the CdTe helix has little impact on the chiroptical response (fig. S10); therefore, the nanowire core was omitted. The CdTe R-helix model structure is as follows: pitch, 650 nm; length, 2600 nm; diameter, 312 nm; and thickness, 25 nm. All the simulations were carried out in effective medium parametrized as water.

Handedness.

Opposite-handed helices exhibited CD and *g* factor spectra with opposite signs (Fig. 4B). This validated our simulation setup, which calculates the absorption and scattering cross sections in response to circularly polarized photons.

Pitch.

Helical pitch length (or the distance for one complete helix turn measured parallel to the helix axis) strongly influences rotatory power. To quantitatively study the effect of pitch on the overall rotatory activity, we constructed five helix models with various pitch lengths (Fig. 4C). The *g* factor reached a maximum at a pitch length of 325 nm. This can be understood by examining the models with the shortest and longest pitches. For helices with 62.5 or 1300 nm pitch lengths, the structure increasingly resembles either a solid cylinder or a rectangular slab respectively, both of which should exhibit no rotatory power. Therefore, it is expected that there is an ideal pitch length for optimal *g* factor

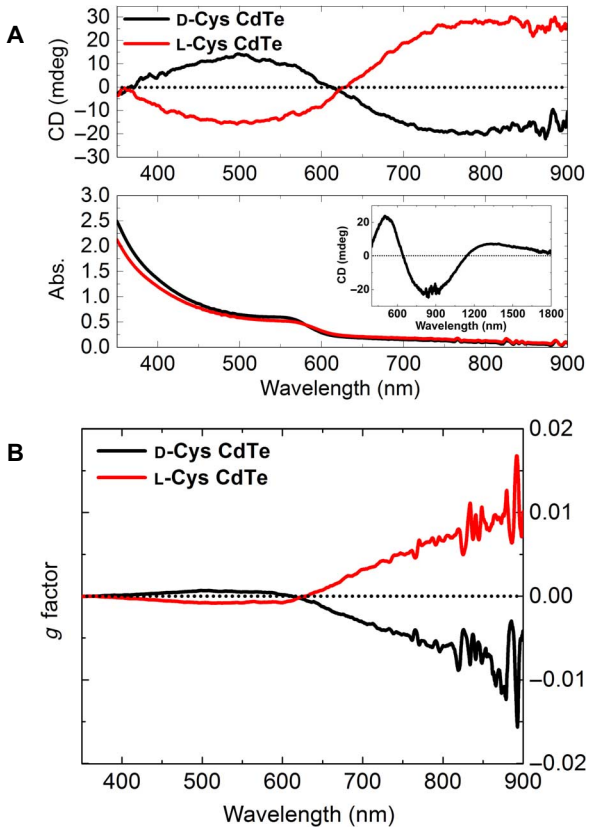

Fig. 3. Chiroptical spectra of mesoscale semiconductor helices. (**A**) CD and absorption (abs.) spectra of D- and L-Cys CdTe assemblies in water (inset shows CD spectra of D-Cys CdTe assemblies in D_2O). (**B**) *g* factor spectra of D- and L-Cys CdTe assemblies.

between these two extremes. The CD spectra shifts moderately to the red as pitch becomes longer.

Length.

The length of the helix does not appear to have a noticeable effect on the wavelengths of extrema in CD spectra (Fig. 4D). Longer helices can be essentially regarded as repeating units of shorter helices. However, as the helix becomes longer, the rotatory power intensifies. Both of these observations are intuitively expected from these structures and serve as benchmarks validating the calculations.

Diameter and thickness.

The CD spectra shift to longer wavelengths with increasing diameter (Fig. 4E). The thickness of the wings of the helix strongly affects the CD spectra (Fig. 4F). Maxima and minima of the CD spectra experience strong redshift as the thickness increases: For every 25-nm increase in thickness, there is a corresponding redshift of ~130 nm. In addition, CD intensity and *g* factor values increase with thickness.

Material.

An in-depth understanding of the differences between semiconducting, metallic, and organic helices is critical for the application-driven design of chiroptical materials. We compared the simulated CD and *g* factor spectra (Fig. 4G) for helices of the same geometrical parameters but computationally "substituted" with materials of various refractive indices (fig. S11). They included semiconductors (CdTe and Si), metals (Au), ceramics (SiO_2), and organic materials [poly(methyl methacrylate) (PMMA)]. Si helices, a semiconductor material, have a bisignate chiroptical response similar to that of CdTe helices. On the

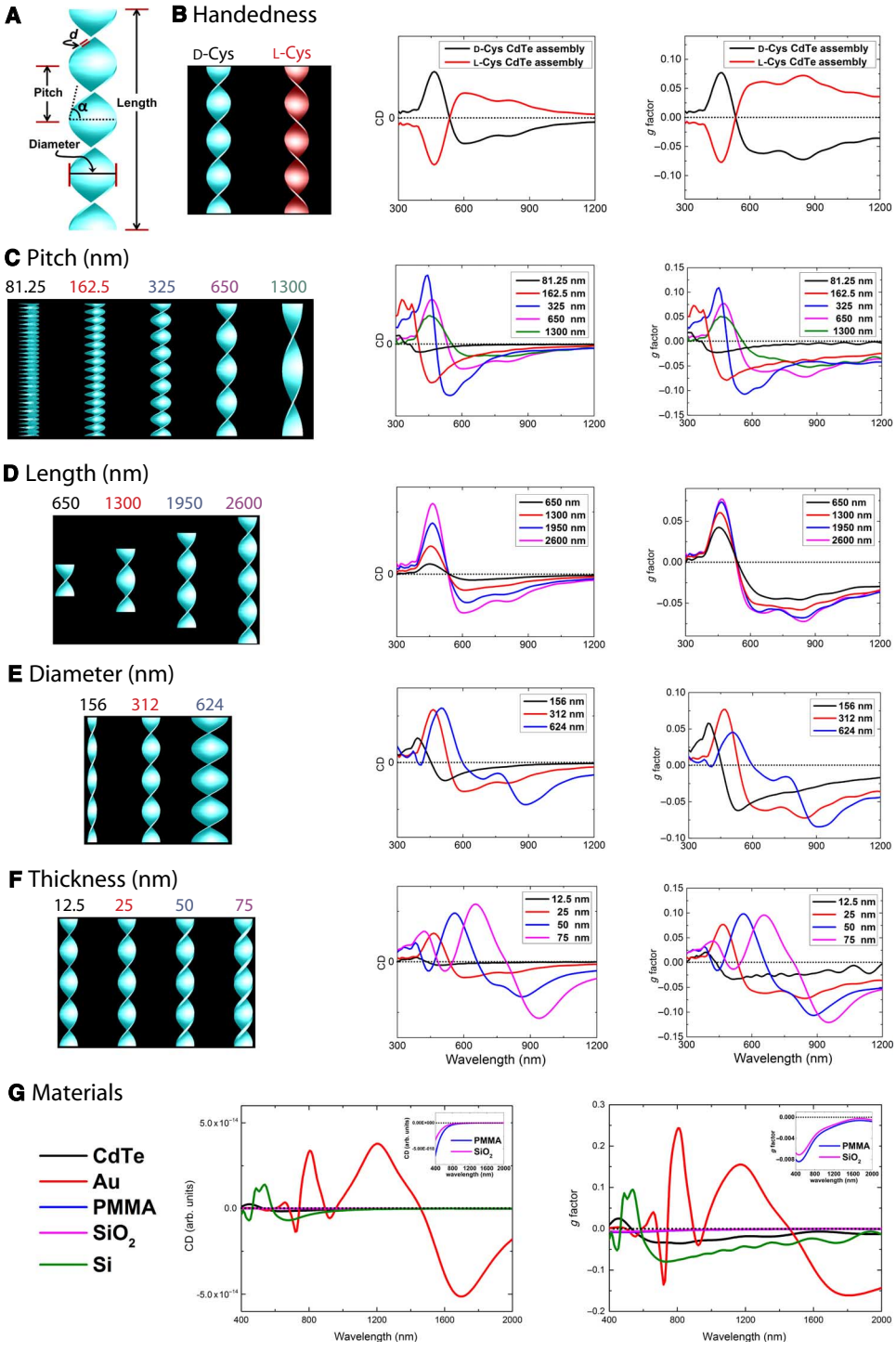

Fig. 4. Structure-property relationships for helices from different classes of materials obtained by DFTD simulations. (**A**) Illustration of the various geometrical parameters in a typical CdTe helix (*d* represents thickness). Simulated CD and *g* factor spectra with geometrical parameters of the variable as follows: (**B**) handedness, (**C**) pitch, (**D**) length, (**E**) diameter, and (**F**) thickness. (**G**) Simulated CD and *g* factor spectra for helices of CdTe, Au, PMMA, SiO_2, and Si. The simulated structure is a right-handed helix (pitch size, 650 nm; length, 325 nm; diameter, 312 nm; and thickness, 25 nm). arb. units, arbitrary units.

other hand, Au helices show significant differences in CD and *g* factor spectra compared to the semiconductor helices. This is due to strong chiroptical responses from multipole plasmon resonances of Au helices (fig. S12) (*62*–*65*).

Ceramic (SiO_2) or polymer (PMMA) helices show weak chiroptical responses due to the small difference in refractive indices (*n* and *k* are the real and imaginary parts of the complex refractive index, respectively) compared to the medium ($n_{SiO2} \approx n_{PMMA} \approx 1.5$; $n_{water} = 1.33$)

and the lack of absorption within the materials ($k_{SiO2} = k_{PMMA} = 0$). Nonracemic SiO_2 helices were reported to yield no observable chiroptical response within instrumental sensitivity (*66*), which strengthens the conclusion that the chiroptical response for SiO_2 helices is weak and verifies the calculations in Fig. 4G.

The relative contribution of the absorption and scattering to chiroptical properties is essential for understanding the chiroptical effects observed here and for other chiral inorganic nanostructures. First, by comparing semiconductor and plasmonic helices of identical geometries, one can see that the absorption/scattering ratio under CPL is significantly different (fig. S13). For CdTe helices, this ratio is 1:1.6 and 1:0.9 for left-handed CPL (LCP) and right-handed CPL (RCP), respectively. When it comes to Au helices, the scattering is much stronger than absorption, with absorption/scattering ratios of 1:5.4 and 1:7.6 under LCP and RCP irradiation, respectively. In the case of ceramic and polymeric helices, scattering is a singular contributor to the chiroptical response, unless the ceramic or polymeric helices are doped with light-adsorbing species. For semiconducting helices, the large contribution of absorption to chiroptical response represents an additional modality in controlling light-matter interaction suitable for fast polarization modulation in optical devices.

Comparison of experimental results and simulations

The geometry (length, diameter, and pitch) of model helices in simulations is based on statistical analysis of SEM images of experimental helices (table S2, figs. S14 and S15). The CD spectra calculated with these geometrical parameters demonstrated a nearly perfect match with experimental CD spectra, reproducing the overall shape, spectral positions, and the peak-to-valley intensity ratio (Fig. 5, A and B). The broader peaks in the experimental spectra are likely due to some polydispersity of the helices in dispersions (*14*).

Experimentally, we observed that for NPs aged for different periods of time, the CD spectra of the resulting self-assembled helices experience a bathochromic shift (Fig. 5, C and D). Simulated CD spectra using averaged geometry data yielded similar redshifts. Taking into account that the two geometries differed mainly in thickness (figs. S15 and S16), it can be concluded that the thickness is the main contributor to this experimental redshift, in agreement with predictions in Fig. 4F. Thickness-dependent chiroptical redshifts have also been reported for Ag deposited on SiO_2 helices (*66*), which matched those calculated in Fig. 4G. These findings and comparisons with literature data further validated the simulation-derived structure-property relationships.

Light-matter interaction

Electric field profiles at select wavelengths can provide additional insight into light-matter interaction (Fig. 6). The strongest electric field enhancement occurred at 691 nm, close to the helical pitch size (650 nm), demonstrating that light-matter interaction is most intense when dimensions of the helices draw close to those of the

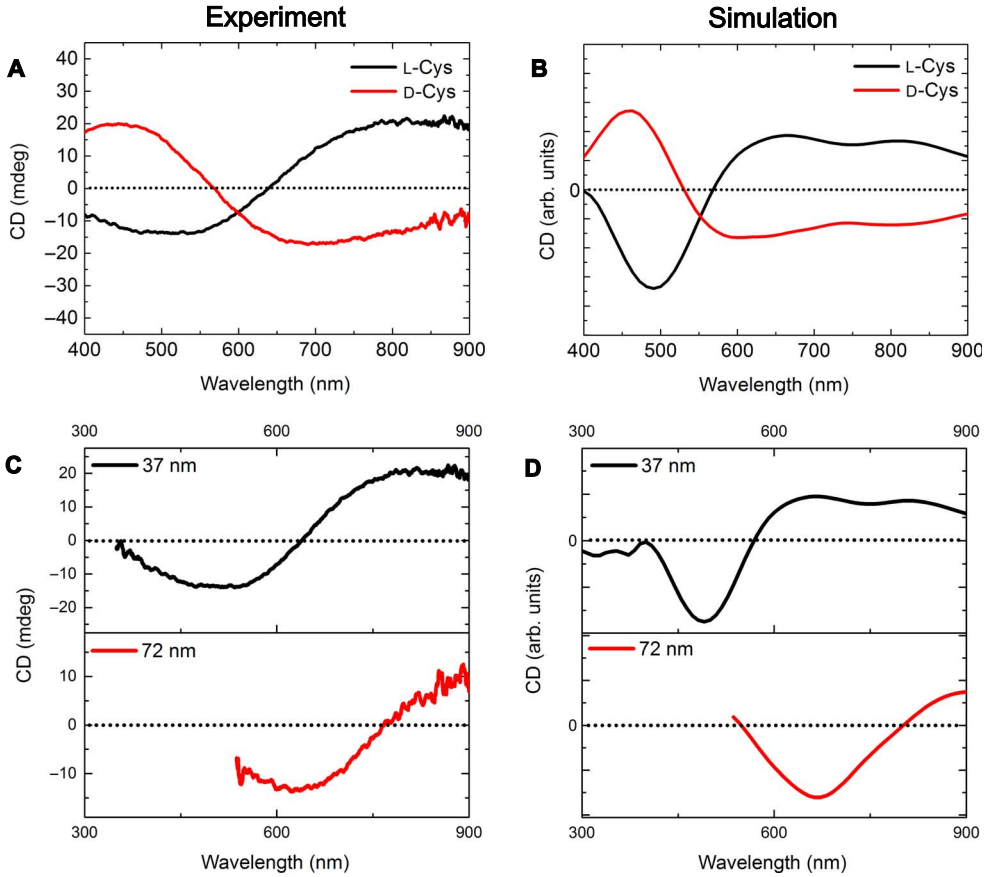

Fig. 5. Experiment-simulation comparison. (**A**) Experimental and (**B**) simulated CD spectra of L- and R-helices. (**C**) Experimental and (**D**) simulated CD spectra of R-helices with a thickness of 37 and 72 nm, respectively.

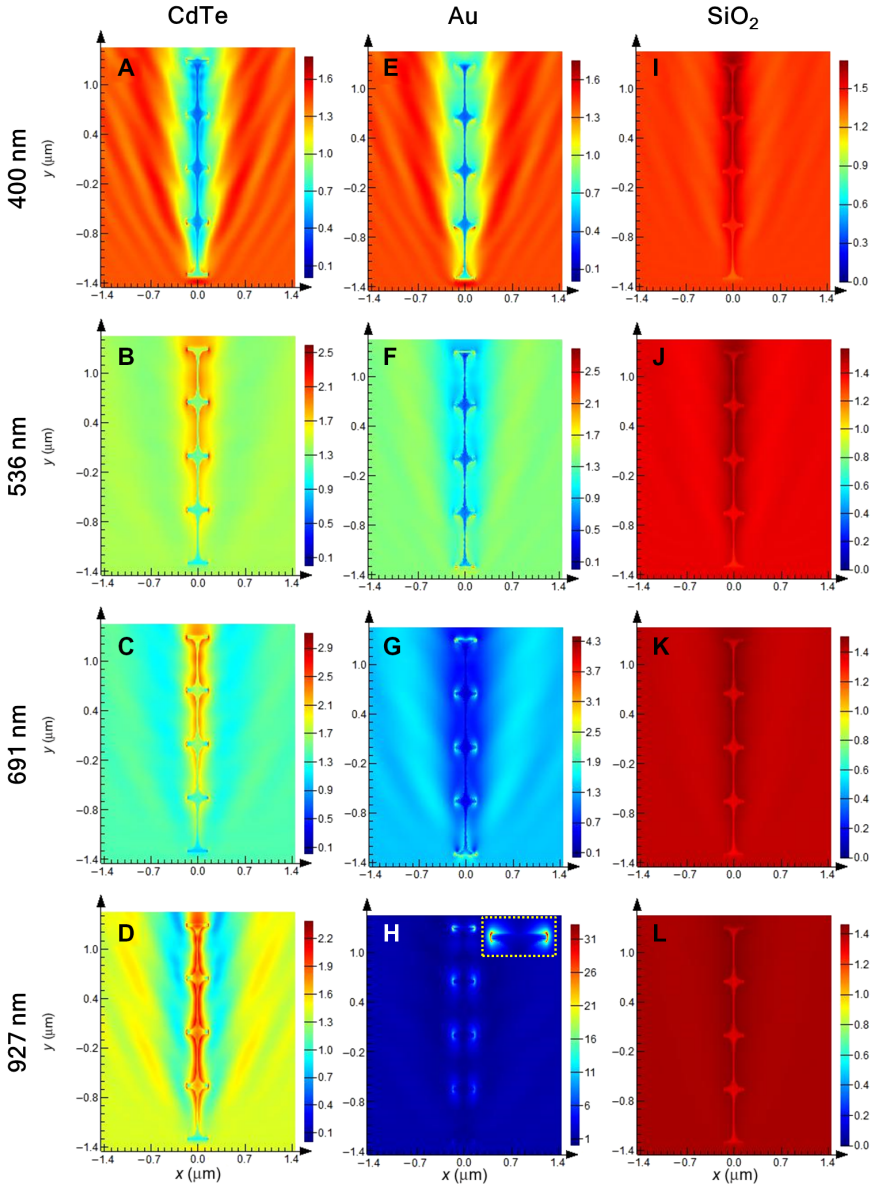

Fig. 6. Electric field profiles. Electric field profiles at the $z = 0$ plane for (**A** to **D**) CdTe, (**E** to **H**) Au, and (**I** to **L**) SiO_2. Four wavelengths (400, 536, 691, and 927 nm) were chosen to represent the entire spectral range. RCP light was injected from bottom to top and parallel to the axis of the helix. Inset in (H) shows the magnified view of the top of the helix. Note the difference in color scales for the different materials and wavelengths.

CPL wavelength. It is informative to compare the electric field profiles generated by a metallic (Au) or ceramic (SiO_2) helix with those generated by CdTe. When an Au helix is subject to CPL irradiation, strong absorption at all wavelengths is observed; when irradiated with 927-nm RCP, the electric field enhancement at the Au helix and water boundary is *ca.* 10 times larger than that for the CdTe helix, most likely due to plasmon resonance (fig. S12). In contrast, ceramic (SiO_2) helices show low electric field enhancement at the helix-water boundary. The comparison of electric field profiles among different helix materials validates the understanding that semiconductor chiral nanomaterials display unique chiroptical features in response to circular polarization compared to their metallic or ceramic counterparts.

Electric field profiles are compiled into time-domain animations of electric field isosurfaces (EFIs), three-dimensional (3D) surface representation of equal electric fields. EFIs curl as the electromagnetic pulse travels along the nanostructure, in addition to gradually losing power as light is absorbed and scattered (movies S3 and S4). The curl direction is dependent on the extrinsic chirality of the helix, demonstrating strong modulation due to the difference of electromagnetic properties between the helix and water. The residual electric field after passing through the helix is different for LCP and RCP: RCP irradiation of R-helices showed weaker residual electric field than LCP (fig. S17). As expected, achiral structures were subject to identical irradiation conditions (movies S5 and S6), and the resulting EFIs appeared to be discrete without curling (fig. S18). The movies permit

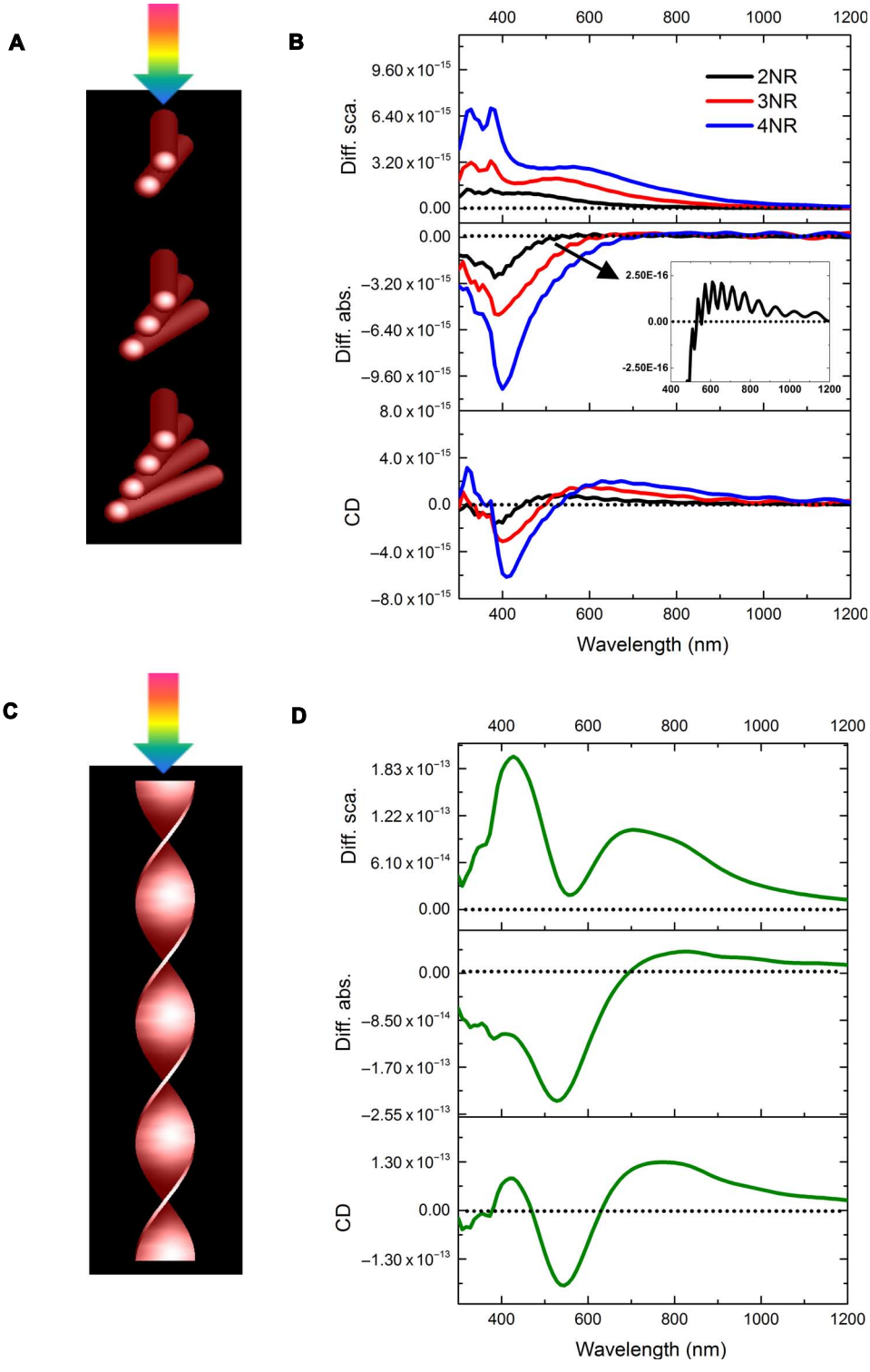

Fig. 7. Simulated nanorod deconstruction of a helix. (**A**) Schematic of CPL irradiating a series of NR dimers (2NR), trimers (3NR), and tetramers (4NR). (**B**) Differential scattering (diff. sca.), differential absorption (diff. abs.) (inset shows a magnified view for dimer), and CD spectra for 2NR, 3NR, and 4NR. (**C**) Schematic of CPL irradiating onto a helix and (**D**) differential scattering, differential absorption, and CD spectra for the helix. Nanorod models are 312, 40, and 4 nm in length, diameter, and internanorod spacing, respectively, with a 10° dihedral angle.

visualization of electric field dynamics in response to variations in chirality of inorganic nano and mesoscale structures.

DISCUSSION

Simplified nanorod model: Dipoles versus multipoles

A helix can be treated as a series of nanorods placed infinitely close and at an angle to each other (Fig. 7A). To understand the CD spectra of a CdTe R-helix, we constructed a series of right-handed CdTe nanorod dimer (2NR), trimer (3NR), and tetramer (4NR) models. If these simplified models could reasonably reproduce the chiroptical spectra of the parent helices, they can then be used to gain physical insight into helix chiroptical properties.

As the number of nanorods increases from two to four, the bisignate CD spectra of the nanorod models are redshifted and increasingly resemble the CD spectrum of the helix (Fig. 7B). This confirms that the deconstruction of a helix into stacked nanorods is valid.

Let us examine the simplest nanorod model, the dimer. CdTe dimer exhibits a bisignate CD spectrum that is similar to that reported for Au nanorod dimers described by the dipole coupling theory (*67*, *68*). It may appear that CdTe and metallic nanorod dimers share similar chiroptical responses; however, further simulations substituting CdTe with metallic nanorods while retaining the original dimensions of the dimers proved these assumptions premature: Both Au and Ag dimers show complex multipole plasmon resonances (fig. S19A). Note that the size and aspect ratio of nanorods (length, 312 nm; width, 40 nm; and aspect ratio ≈ 8:1) used in these simulations were larger than those previously used in many other studies. At this specific size and aspect ratio regime, multipole plasmon resonances gain provenance (*62*–*65*); therefore, the dipolar model that predicts a simple bisignate CD spectrum becomes inaccurate.

Contrary to the multipole plasmon resonances observed for metallic dimers, semiconductor dimers of various materials (CdTe, Si, or GaAs) all produced a bisignate CD spectral shape (fig. S19B). This arises from the inability of semiconductors to generate multipole resonances even at large sizes and aspect ratios, because semiconductors generally have lower free-electron density compared to metals (*69*).

Outlook

A detailed understanding of how semiconductor helical nanostructures interact with light and the design parameters for engineering their optical response emerged from this study. Chiral semiconductor mesoscale helices demonstrated unique chiroptical properties compared to metallic, ceramic, or polymeric ones. Rotatory optical activity of semiconductor helices has large contribution from light absorption, which makes them, to some degree, similar to the chiral organic molecules, albeit with much greater rotatory power. The chiroptical properties of helices can be modulated by various geometrical parameters such as pitch length, diameter, and thickness. Among these parameters, thickness is the most significant parameter in spectral wavelength modulation, followed by diameter and pitch. These parameters can be tuned by controlling interparticle interactions to design high-performance chiroptical materials, combining high *g* factor and field modulation. The possibility of such control can be inferred from this and previous work (*15*–*35*), laying the groundwork for future development.

Chiral self-sorting represents an important characteristic for this self-assembly system, ensuring the efficient transfer of chirality from small molecules to the mesoscale, owing to thermodynamically preferred assembly of NPs with the same handedness. Because inorganic NPs were likely present in the environment of primordial Earth (*70*), the finding that simple chiral ligands control the assembly of semiconductor NPs into homochiral helices could play a role in explaining the origin of homochirality on Earth.

This study will facilitate the development of chiral semiconductor nanostructures with tunable, geometry-dependent chiroptical activity and broadband Vis-NIR characteristics. The combination of the relatively large *g* factor and field-variable absorption characteristics of the semiconductors creates the grounds for further development of polarization-based biomedical diagnostics (*45*), hyperspectral sensors (*47*), telecommunication (*71*), and short-wave infrared imaging (*72*).

MATERIALS AND METHODS

Synthesis of Cys-CdTe NPs

The synthetic procedure was adapted from a previous report by Gaponik *et al.* (*73*). Briefly, $Cd(ClO_4)_2{\cdot}6H_2O$ (0.985 g) and D- or L-cysteine hydrochloride monohydrate (0.990 g) were dissolved in 125 ml of deionized water, followed by adjusting the pH to 11.2 with 1 M NaOH. This solution was placed in a three-neck, round-bottom flask and purged with N_2 for 30 min. H_2Te gas (generated by reacting 0.05 to 0.10 g of Al_2Te_3 with 10 ml of 0.5 M H_2SO_4) was slowly passed through the solution. The solution was then allowed to reflux under N_2 at 100°C for 60 min to obtain the Cys-CdTe NPs used in this work. For storage, the NP solution was thoroughly purged with N_2 for at least 30 min and then kept in the dark at 4°C.

For both D- and L-Cys CdTe NPs, TEM analysis showed similar size distribution and electron diffraction where the observed d-spacing exists in both zinc blende (cubic) and wurtzite (hexagonal) structures, with the zinc blende structure being predominant (fig. S20). The size of the NPs was ~3.2 nm. The size was further confirmed by empirical fitting functions (*74*) with the wavelength of the first excitonic absorption peak (~550 nm).

Preparation of helical assemblies

An aging process of the original aqueous NP solution was found to be critical for the preparation of helical assemblies. Assembly into helices only occurred when the original NP dispersion was allowed to age under dark conditions at 4°C for 1 day or more. Residual oxygen is likely to react with NPs. Black precipitates could be observed at the bottom of the container as aging proceeded. The aging process, accompanied by a decrease in NP size, could be followed spectrally by a blueshift of the first excitonic absorption peak (fig. S21). The rotatory power of the NPs appeared relatively stable over the same period (fig. S22).

When the NPs were sufficiently aged to be assembled, a solvent exchange step was performed to transfer the NPs from water to methanol. The NP aqueous dispersion and methanol were mixed at a volume ratio of 1:1.5 to precipitate the NPs. This solution was then placed in a centrifuge at 1500 rpm for 3 min, the supernatant was discarded, and the precipitate was redispersed in methanol. At this point, the excess Cys ligand was removed, and the NPs were considered to be "activated" for assembly. The assembly process was usually allowed to proceed overnight, unless explicitly noted otherwise.

For CD measurements, the as-assembled helices in methanol were transferred to water, where they were dispersed with ease. The methanol dispersion was placed in a centrifuge at 1500 rpm for 3 min. We discarded the supernatant, and redispersed the precipitate in water. This aqueous dispersion was then subjected to another centrifugation step (2000 rpm for 3 min), with the supernatant being

used for the CD studies (this additional centrifuge step was skipped for formation mechanism studies presented in Fig. 2, A to K). The procedure for the preparation of helical assemblies is illustrated in schematic S1. D_2O was used as the solvent instead of water for the NIR CD measurement shown in the inset of Fig. 3A because D_2O absorbs less in the infrared region than water and, therefore, is ideal for CD data collection with a wider usable wavelength range.

CD instrumentation

JASCO J-815 [two photomultiplier (PMT) detectors with 200 to 900 and 700 to 1100 nm ranges] and J-1700 (one PMT detector with a 200-800 nm range and two InGaAs NIR detectors with 800 to 1600 and 1600 to 2500 nm ranges) CD spectrophotometers were used for the CD studies. Typical scanning parameters were as follows: scanning speed, 100 nm/min; data pitch, 0.1 nm; bandwidth, 1 nm (NIR bandwidth, 20 nm), digital integration time, 4 s; and one accumulation. The anisotropy (g) factor was calculated according to the following equation: $g = \frac{CD}{32{,}980 \times abs.} = 0.0000303214 \times \frac{CD}{abs.}$. CD spectra were stopped at wavelengths where the high tension voltage on the PMT detector exceeded the maximum (800 V) allowed for reliable CD data collection.

Imaging

FEI Nova 200 Nanolab Dualbeam SEM was used for SEM imaging and EDX elemental analysis. JEOL 3011 was used for TEM imaging and SAED analysis. JEOL 2100F was used for STEM imaging and EDX elemental analysis. A tomogram reconstruction software (eTomo) and a visualization software (Amira) were used to generate 3D tomography.

ITC studies

A TA Instruments Nano ITC Low Volume isothermal titration calorimeter was used. The excess ligand in the original NP aqueous solution was removed by centrifugation at 1500 rpm for 3 min and the NPs were then redispersed in water. Both D- and L-Cys CdTe NPs had the same size (3.2 nm), concentration (0.02 mM), and pH value (9.9). The NP solution in the sample cell and the syringe had the same concentration (0.02 mM). The syringe volume was 50 μl, with 2.5 μl per injection (20 injections in total) and an injection interval of 150 s. An initial baseline was collected for 100 s before the first injection. The temperature was set to 22°C. The stirring rate was 350 rpm. NanoAnalyze software was used to analyze the raw heat rate graphs and to model with a constant blank model and an independent model.

Simulations

The CD and g factor spectra were calculated using a commercial FDTD software package (Lumerical Solutions Inc.; www.lumerical.com/tcad-products/fdtd/). We used total-field scattered-field (TFSF) sources that surrounded the structure being modeled. CPL was generated by positioning two TFSF sources along the same forward axis at a 90° angle and with a phase difference of either −90° (LCP) or 90° (RCP). Two analysis groups using box power monitors monitored the absorption and scattering cross sections (extinction is the sum of absorption and scattering). The FDTD simulation region was defined by a larger box monitor with a stretched-coordinate perfectly matched layer and nonuniform mesh type. Frequency profile monitors were inserted in the total field region to calculate electric field enhancement in 2D. The accuracy of the simulation model was verified and validated with a chiral gold nanorod dimer structure reported in the study of Ma *et al.* (*5*), where the simulated CD spectrum (fig. S23) produced an excellent match with the experimental one with positive-negative bisignate wave shape at similar wavelength region. The refractive index for water was 1.33. The refractive index of Te was adapted from the study of Verbeiren *et al.* (*75*). The refractive index for CdTe was derived from the Sopra Material Database (http://sspectra.com/sopra.html). Another CdTe refractive index data set derived from individual CdTe NPs (with first excitonic absorption peak at 550 nm) was used to simulate light-matter interaction of a helix (see refractive index data sets in fig. S11). These failed to yield the characteristic bisignate shape of the CD spectra observed experimentally (fig. S24). This discrepancy is attributed to the effect of exciton confinement, which is much more pronounced for NPs.

Helices adopt random orientations during CD measurement; therefore, simulations took this into account (except when explicitly stated otherwise). Simulations of randomized orientation were achieved as follows: The helix was allowed to rotate along the y axis every 30° from 0° to 150° and along the z axis every 30° from 0° to 330°, and the final CD and g factor spectra were averaged over a total of 72 orientations (multiplication of 6 rotations along the y axis and 12 rotations along the z axis). Convergence tests with different mesh sizes were performed to determine the best balance between computational time restraints and simulation accuracy. Simulations on one orientation of the CdTe helices (CPL on axis with helix) with 25- or 10-nm mesh size produced similar CD spectra; therefore, we used 25-nm mesh size for CdTe helix simulations. There is an exception to this mesh size in constructing electric field profiles, where a finer mesh size of 5 nm was adopted to enhance the profile resolution.

In the computations designed to elucidate the effect of refractive indices, the simulated structure was a right-handed helix (pitch size, 650 nm; length, 325 nm; diameter, 312 nm; and thickness, 25 nm). The relatively small model size was intended to reduce the computational time. Note that small mesh sizes and longer simulation times were required to provide accurate results for Au. Convergence tests with three different mesh sizes of 5, 2.5, or 1.25 nm yielded very similar CD spectra, indicating that a mesh size of 5 nm was sufficient for accurate simulations.

The mesh size for nanorod models (2NR, 3NR, and 4NR) was 0.5 nm, although a larger mesh size, such as 1 nm, did not yield significantly different spectra. 3D animations of EFIs were produced in ParaView, using electric field vector values derived from Lumerical simulations.

SUPPLEMENTARY MATERIALS

Supplementary material for this article is available at http://advances.sciencemag.org/cgi/content/full/3/3/e1601159/DC1

fig. S1. Assembly from TGA-CdTe NPs.
fig. S2. Helical structure of opposite handedness found among helices assembled from L-Cys CdTe NPs.
fig. S3. Chiroptical spectra of different NP assemblies.
fig. S4. ITC data for chiral interactions and their fitting with thermodynamic models.
fig. S5. Long-term stability of homochiral mesoscale helices.
fig. S6. CdS nanofibers observed after long-term storage of the CdTe NP dispersions.
fig. S7. Contribution of random aggregates to the overall chiroptical activity.
fig. S8. Vis-NIR chiroptical response of mesoscale helices.
fig. S9. CD and absorption spectra of CdTe NPs.
fig. S10. Calculated CD spectra of CdTe helix with or without a Te nanowire core.
fig. S11. Refractive index data sets.
fig. S12. Extinction spectrum of Au helices.
fig. S13. Absorption and scattering spectra of Au and CdTe helices.
figs. S14 to S16. Helix thickness.
figs. S17 and S18. EFI movie snapshots.
fig. S19. Nanorod dimer simulations.
fig. S20. TEM images and crystal lattice of CdTe NPs.
fig. S21. Absorption spectra of CdTe NPs during aging.

fig. S22. CD spectra of CdTe NPs during aging.
fig. S23. Verification of the computational model.
fig. S24. Simulations using CdTe NP refractive index.
schematic S1. Experimental methods.
schematic S2. Schematic drawing of an "untwisted" helix.
table S1. Statistical analysis of racemic NP assemblies.
table S2. Statistical analysis of geometrical parameters of helices obtained from SEM images.
table S3. Percent yield calculations.
movie S1. R-helix in 3D rotating view.
movie S2. L-helix in 3D rotating view.
movie S3. RCP irradiation on an R-helix.
movie S4. RCP irradiation on an L-helix.
movie S5. RCP irradiation on an achiral ribbon.
movie S6. LCP irradiation on an achiral ribbon.
section S1. Percent yield.

REFERENCES AND NOTES

1. R. Janoschek, *Chirality: From Weak Bosons to the α-helix* (Springer-Verlag, 1991).
2. H.-S. Kitzerow, *Chirality in Liquid Crystals* (Springer-Verlag, 2001).
3. N. Berova, K. Nakanishi, R. W. Woody, *Circular Dichroism: Principles and Applications* (Wiley-VCH, 2000).
4. X. Wu, L. Xu, L. Liu, W. Ma, H. Yin, H. Kuang, L. Wang, C. Xu, N. A. Kotov, Unexpected chirality of nanoparticle dimers and ultrasensitive chiroplasmonic bioanalysis. *J. Am. Chem. Soc.* **135**, 18629–18636 (2013).
5. W. Ma, H. Kuang, L. Xu, L. Ding, C. Xu, L. Wang, N. A. Kotov, Attomolar DNA detection with chiral nanorod assemblies. *Nat. Commun.* **4**, 2689 (2013).
6. A. Sharma, T. Mori, H.-C. Lee, M. Worden, E. Bidwell, T. Hegmann, Detecting, visualizing, and measuring gold nanoparticle chirality using helical pitch measurements in nematic liquid crystal phases. *ACS Nano* **8**, 11966–11976 (2014).
7. Y. Wang, J. Xu, Y. Wang, H. Chen, Emerging chirality in nanoscience. *Chem. Soc. Rev.* **42**, 2930–2962 (2013).
8. W. Yan, L. Xu, C. Xu, W. Ma, H. Kuang, L. Wang, N. A. Kotov, Self-assembly of chiral nanoparticle pyramids with strong R/S optical activity. *J. Am. Chem. Soc.* **134**, 15114–15121 (2012).
9. T. Hu, B. P. Isaacoff, J. H. Bahng, C. Hao, Y. Zhou, J. Zhu, X. Li, Z. Wang, S. Liu, C. Xu, J. S. Biteen, N. A. Kotov, Self-organization of plasmonic and excitonic nanoparticles into resonant chiral supraparticle assemblies. *Nano Lett.* **14**, 6799–6810 (2014).
10. A. Kuzyk, R. Schreiber, Z. Fan, G. Pardatscher, E.-M. Roller, A. Högele, F. C. Simmel, A. O. Govorov, T. Liedl, DNA-based self-assembly of chiral plasmonic nanostructures with tailored optical response. *Nature* **483**, 311–314 (2012).
11. J. K. Gansel, J. K. Gansel, M. Thiel, M. S. Rill, M. Decker, K. Bade, V. Saile, G. Von Freymann, S. Linden, M. Wegener, Gold helix photonic metamaterial as broadband circular polarizer. *Science* **1513**, 1513–1515 (2009).
12. J. Govan, and Y. K. Gun'ko, Recent progress in chiral inorganic nanostructures. *Nanoscience* **3**, 1–30 (2016).
13. A. Kuzyk, R. Schreiber, H. Zhang, A. O. Govorov, T. Liedl, N. Liu, Reconfigurable 3D plasmonic metamolecules. *Nat. Mater.* **13**, 862–866 (2014).
14. A. Guerrero-Martínez, B. Auguié, J. L. Alonso-Gómez, Z. Džolić, S. Gómez-Graña, M. Žinić, M. M. Cid, L. M. Liz-Marzán, Intense optical activity from three-dimensional chiral ordering of plasmonic nanoantennas. *Angew. Chem. Int. Ed. Engl.* **50**, 5499–5503 (2011).
15. J. Yeom, B. Yeom, H. Chan, K. W. Smith, S. Dominguez-Medina, J. H. Bahng, G. Zhao, W.-S. Chang, S.-J. Chang, A. Chuvilin, D. Melnikau, A. L. Rogach, P. Zhang, S. Link, P. Král, N. A. Kotov, Chiral templating of self-assembling nanostructures by circularly polarized light. *Nat. Mater.* **14**, 66–72 (2014).
16. M. Hentschel, M. Schäferling, T. Weiss, N. Liu, H. Giessen, Three-dimensional chiral plasmonic oligomers. *Nano Lett.* **12**, 2542–2547 (2012).
17. W. Chen, A. Bian, A. Agarwal, L. Lui, H. Shen, L. Wang, C. Xu, A. Kotov, Nanoparticle superstructures made by polymerase chain reaction: Collective interactions of nanoparticles and a new principle for chiral materials. *Nano Lett* **9**, 2153–2159 (2009).
18. A. G. Mark, J. G. Gibbs, T.-C. Lee, P. Fischer, Hybrid nanocolloids with programmed three-dimensional shape and material composition. *Nat. Mater.* **12**, 802–807 (2013).
19. K. Sawai, R. Tatumi, T. Nakahodo, H. Fujihara, Asymmetric Suzuki-Miyaura coupling reactions catalyzed by chiral palladium nanoparticles at room temperature. *Angew. Chem. Int. Ed. Engl.* **47**, 6917–6919 (2008).
20. C. Gautier, T. Bürgi, Chiral *N*-isobutyryl-cysteine protected gold nanoparticles: Preparation, size selection, and optical activity in the UV–vis and infrared. *J. Am. Chem. Soc.* **128**, 11079–11087 (2006).
21. V. E. Ferry, J. M. Smith, A. P. Alivisatos, Symmetry breaking in tetrahedral chiral plasmonic nanoparticle assemblies. *ACS Photonics* **1**, 1189–1196 (2014).
22. Z. Fan, A. O. Govorov, Plasmonic circular dichroism of chiral metal nanoparticle assemblies. *Nano Lett.* **10**, 2580–2587 (2010).
23. X. Lan, Q. Wang, Self-Assembly of Chiral Plasmonic Nanostructures. *Adv. Mater.* **28**, 10499–10507 (2006).
24. H. Matsukizono, R.-H. Jin, High-temperature-resistant chiral silica generated on chiral crystalline templates at neutral pH and ambient conditions. *Angew. Chem. Int. Ed. Engl.* **51**, 5862–5865 (2012).
25. B. Liu, L. Han, Y. Duan, Y. Cao, J. Feng, Y. Yao, S. Che, Growth of optically active chiral inorganic films through DNA self-assembly and silica mineralisation. *Sci. Rep.* **4**, 4866 (2014).
26. E. L. Ivchenko, B. Spivak, Chirality effects in carbon nanotubes. *Phys. Rev. B.* **66**, 155404 (2002).
27. A. Sánchez-Castillo, C. E. Román-Velázquez, C. Noguez, Optical circular dichroism of single-wall carbon nanotubes. *Phys. Rev. B.* **73**, 045401 (2006).
28. S. Liu, Y. Duan, X. Feng, J. Yang, S. Che, Synthesis of enantiopure carbonaceous nanotubes with optical activity. *Angew. Chem. Int. Ed. Engl.* **52**, 6858–6862 (2013).
29. S. D. Elliott, M. P. Moloney, Y. K. Gun'ko, Chiral shells and achiral cores in CdS quantum dots. *Nano Lett.* **8**, 2452–2457 (2008).
30. M. V. Mukhina, V. G. Maslov, A. V. Baranov, A. V. Fedorov, A. O. Orlova, F. Purcell-Milton, J. Govan, Y. K. Gun'ko, Intrinsic chirality of CdSe/ZnS quantum dots and quantum rods. *Nano Lett.* **15**, 2844–2851 (2015).
31. A. S. Baimuratov, I. D. Rukhlenko, Y. K. Gun'ko, A. V. Baranov, A. V. Fedorov, Dislocation-induced chirality of semiconductor nanocrystals. *Nano Lett.* **15**, 1710–1715 (2015).
32. Y. Zhou, M. Yang, K. Sun, Z. Tang, N. A. Kotov, Similar topological origin of chiral centers in organic and nanoscale inorganic structures: Effect of stabilizer chirality on optical isomerism and growth of CdTe nanocrystals. *J. Am. Chem. Soc.* **132**, 6006–6013 (2010).
33. C. Tan, X. Qi, Z. Liu, F. Zhao, H. Li, X. Huang, L. Shi, B. Zheng, X. Zhang, L. Xie, Z. Tang, W. Huang, H. Zhang, Self-assembled chiral nanofibers from ultrathin low-dimensional nanomaterials. *J. Am. Chem. Soc.* **137**, 1565–1571 (2015).
34. C. A. Silvera Batista, R. G. Larson, N. A. Kotov, Nonadditivity of nanoparticle interactions. *Science* **350**, 1242477 (2015).
35. Y. Zhou, R. Marson, G. van Anders, J. Zhu, G. Ma, P. Ercius, K. Sun, B. Yeom, S. C. Glotzer, N. A. Kotov, Biomimetic hierarchical assembly of helical supraparticles from chiral nanoparticles. *ACS Nano* **10**, 3248–3256 (2016).
36. M. Liu, L. Zhang, T. Wang, Supramolecular chirality in self-assembled systems. *Chem. Rev.* **115**, 7304–7397 (2015).
37. A. Samanta, Z. Liu, S. K. M. Nalluri, Y. Zhang, G. C. Schatz, J. F. Stoddart, Supramolecular double-helix formation by diastereoisomeric conformations of configurationally enantiomeric macrocycles. *J. Am. Chem. Soc.* **138**, 14469–14480 (2016).
38. E. Yashima, N. Ousaka, D. Taura, K. Shimomura, T. Ikai, K. Maeda, Supramolecular helical systems: Helical assemblies of small molecules, foldamers, and polymers with chiral amplification and their functions. *Chem. Rev.* **116**, 13752–13990 (2016).
39. P. X. Gao, Y. Ding, W. Mai, W. L. Hughes, C. Lao, Z. L. Wang, Conversion of zinc oxide nanobelts into superlattice-structured nanohelices. *Science* **309**, 1700–1704 (2005).
40. D. Moore, Y. Ding, Z. L. W. Zhong, Hierarchical structured nanohelices of ZnS. *Angew. Chem. Int. Ed. Engl.* **45**, 5150–5154 (2006).
41. G. Z. Shen, Y. Bando, C. Y. Zhi, X. L. Yuan, T. Sekiguchi, D. Golberg, Single-crystalline cubic structured InP nanosprings. *Appl. Phys. Lett.* **88**, 243106 (2006).
42. V. Y. Prinz, V. A. Seleznev, A. K. Gutakovsky, A. V. Chehovskiy, V. V. Preobrazhenskii, M. A. Putyato, T. A. Gavrilova, Free-standing and overgrown InGaAs/GaAs nanotubes, nanohelices and their arrays. *Physica. E* **6**, 828–831 (2000).
43. E. D. Sone, E. R. Zubarev, S. I. Stupp, Semiconductor nanohelices templated by supramolecular ribbons. *Angew. Chem. Int. Ed.* **41**, 1705–1709 (2002).
44. V. I. Kopp, V. M. Churikov, J. Singer, N. Chao, D. Neugroschl, A. Z. Genack, Chiral fiber gratings. *Science* **305**, 74–75 (2004).
45. A. M. Smith, M. C. Mancini, S. Nie, Bioimaging: Second window for in vivo imaging. *Nat. Nanotechnol.* **4**, 710–711 (2009).
46. X. Michalet, F. F. Pinaud, L. A. Bentolila, J. M. Tsay, S. Doose, J. J. Li, G. Sundaresan, A. M. Wu, S. S. Gambhir, S. Weiss, Quantum dots for live cells, in vivo imaging, and diagnostics. *Science* **307**, 538–544 (2005).
47. D. J. Mulla, Twenty five years of remote sensing in precision agriculture: Key advances and remaining knowledge gaps. *Biosyst. Eng.* **114**, 358–371 (2013).
48. S. Che, Z. Liu, T. Ohsuna, K. Sakamoto, O. Terasaki, T. Tatsumi, Synthesis and characterization of chiral mesoporous silica. *Nature* **429**, 281–284 (2004).
49. G. Singh, H. Chan, A. Baskin, E. Gelman, N. Repnin, P. Král, R. Klajn, Self-assembly of magnetite nanocubes into helical superstructures. *Science* **345**, 1149–1153 (2014).
50. Z. Tang, Y. Wang, K. Sun, N. A. Kotov, Spontaneous transformation of stabilizer-depleted binary semiconductor nanoparticles into selenium and tellurium nanowires. *Adv. Mater.* **17**, 358–363 (2005).
51. Z. Tang, Y. Wang, S. Shanbhag, M. Giersig, N. A. Kotov, Spontaneous transformation of CdTe nanoparticles into angled Te nanocrystals: From particles and rods to checkmarks, X-marks, and other unusual shapes. *J. Am. Chem. Soc.* **128**, 6730–6736 (2006).

52. M. M. Safont-Sempere, G. Fernández, F. Würthner, Self-sorting phenomena in complex supramolecular systems. *Chem. Rev.* **111**, 5784–5814 (2011).
53. B. Adhikari, J. Nanda, A. Banerjee, Multicomponent hydrogels from enantiomeric amino acid derivatives: Helical nanofibers, handedness and self-sorting. *Soft Matter* **7**, 8913–8922 (2011).
54. C. Roche, H.-J. Sun, M. E. Prendergast, P. Leowanawat, B. E. Partridge, P. A. Heiney, F. Araoka, R. Graf, H. W. Spiess, X. Zeng, G. Ungar, V. Percec, Homochiral columns constructed by chiral self-sorting during supramolecular helical organization of hat-shaped molecules. *J. Am. Chem. Soc.* **136**, 7169–7185 (2014).
55. D. M. Hall, I. R. Bruss, J. R. Barone, G. M. Grason, Morphology selection via geometric frustration in chiral filament bundles. *Nat. Mater.* **15**, 727–732 (2016).
56. T. Koga, M. Matsuoka, N. Higashi, Structural control of self-assembled nanofibers by artificial β-sheet peptides composed of D- or L-isomer. *J. Am. Chem. Soc.* **127**, 17596–17597 (2005).
57. A. Klug, The tobacco mosaic virus particle: Structure and assembly. *Philos. Trans. R Soc. Lond. B Biol. Sci.* **354**, 531–535 (1999).
58. E. Yashima, K. Maeda, Chirality-responsive helical polymers. *Macromolecules* **41**, 3–12 (2008).
59. Z. Tang, N. A. Kotov, M. Giersig, Spontaneous organization of single CdTe nanoparticles into luminescent nanowires. *Science* **297**, 237–240 (2002).
60. P. McPhie, Circular dichroism studies on proteins in films and in solution: Estimation of secondary structure by *g*-factor analysis. *Anal. Biochem.* **293**, 109–119 (2001).
61. B. A. San Jose, S. Matsushita, K. Akagi, Lyotropic chiral nematic liquid crystalline aliphatic conjugated polymers based on disubstituted polyacetylene derivatives that exhibit high dissymmetry factors in circularly polarized luminescence. *J. Am. Chem. Soc.* **134**, 19795–19807 (2012).
62. B. N. Khlebtsov, N. G. Khlebtsov, Multipole plasmons in metal nanorods: Scaling properties and dependence on particle size, shape, orientation, and dielectric environment. *J. Phys. Chem. C* **111**, 11516–11527 (2007).
63. E. K. Payne, K. L. Shuford, S. Park, G. C. Schatz, C. A. Mirkin, Multipole plasmon resonances in gold nanorods. *J. Phys. Chem. B* **110**, 2150–2154 (2006).
64. I. O. Sosa, C. Noguez, R. G. Barrera, Optical properties of metal nanoparticles with arbitrary shapes. *J. Phys. Chem. B* **107**, 6269–6275 (2003).
65. C. Noguez, Surface plasmons on metal nanoparticles: The influence of shape and physical environment. *J. Phys. Chem. C* **111**, 3806–3819 (2007).
66. J. H. Singh, G. Nair, A. Ghosh, A. Ghosh, Wafer scale fabrication of porous three-dimensional plasmonic metamaterials for the visible region: Chiral and beyond. *Nanoscale* **5**, 7224–7228 (2013).
67. L.-Y. Wang, K. W. Smith, S. Dominguez-Medina, N. Moody, J. M. Olson, H. Zhang, W.-S. Chang, N. A. Kotov, S. Link, Circular differential scattering of single chiral self-assembled gold nanorod dimers. *ACS Photonics* **2**, 1602–1610 (2015).
68. B. Auguié, J. L. Alonso-Gómez, A. Guerrero-Martínez, L. M. Liz-Marzán, Fingers crossed: Optical activity of a chiral dimer of plasmonic nanorods. *J. Phys. Chem. Lett.* **2**, 846–851 (2011).
69. A. Kahn, Fermi level, work function and vacuum level. *Mater. Horiz.* **3**, 7–10 (2016).
70. A. Y. Mulkidjanian, On the origin of life in the zinc world: 1. Photosynthesizing, porous edifices built of hydrothermally precipitated zinc sulfide as cradles of life on Earth. *Biol. Direct.* **4**, 26 (2009).
71. Z. Y. Wang, *Near-Infrared Organic Materials and Emerging Applications* (CRC Press, 2013).
72. R. G. Driggers, V. Hodgkin, R. Vollmerhausen, in *Proc. SPIE 8706, Infrared Imaging Systems: Design, Analysis, Modeling, and Testing XXIV* (2013), p. 87060L.
73. N. Gaponik, D. V. Talapin, A. L. Rogach, K. Hoppe, E. V. Shevchenko, A. Kornowski, A. Eychmüller, H. Weller, Thiol-capping of CdTe nanocrystals: An alternative to organometallic synthetic routes. *J. Phys. Chem. B* **106**, 7177–7185 (2002).
74. W. W. Yu, L. Qu, W. Guo, X. Peng, Experimental determination of the extinction coefficient of CdTe, CdSe, and CdS nanocrystals. *Chem. Mater.* **15**, 2854–2860 (2003).
75. P. Verbeiren, F. Dumont, C. Buess-Herman, Determination of the complex refractive index of bulk tellurium and its use in particle size. *Progr. Colloid Polym. Sci.* **100**, 112–116 (1996).

Acknowledgments: We would like to thank W. Zhang for assistance with indexing electron diffraction patterns, E. Mutlugun for providing the refractive index data for individual CdTe NPs, and the University of Michigan's Michigan Center for Materials Characterization for assistance with electron microscopy. **Funding:** The central part of this work was supported by the NSF project "Energy- and Cost-Efficient Manufacturing Employing Nanoparticles" (NSF 1463474). Partial support of this work was also made by the Center for Photonic and Multiscale Nanomaterials funded by the NSF Materials Research Science and Engineering Center program DMR-1120923, as well as NSF projects 1403777 and 1411014, and the University of Michigan's Michigan Center for Materials Characterization for the NSF grant DMR-9871177 for the funding of the JEOL 2100F and 3011 analytical electron microscope used in this work. **Author contributions:** W.F. and J.-Y.K. carried out CdTe NP synthesis, assembly, and characterization. W.F., X.W., and H.A.C. performed Lumerical simulations. W.F. and Z.Q. studied 3D tomography of helices. L.M. carried out TEM studies on CdTe NPs. N.A.K. supervised the project. W.F. and N.A.K. analyzed the data and co-wrote the paper. All authors discussed the results and commented on the manuscript. **Competing interests:** The authors declare that they have no competing interests. **Data and materials availability:** All data needed to evaluate the conclusions in the paper are present in the paper and/or the Supplementary Materials. Additional data related to this paper may be requested from N.A.K. (kotov@umich.edu).

Submitted 22 May 2016
Accepted 15 December 2016
Published 1 March 2017
10.1126/sciadv.1601159

Citation: W. Feng, J.-Y. Kim, X. Wang, H. A. Calcaterra, Z. Qu, L. Meshi, N. A. Kotov, Assembly of mesoscale helices with near-unity enantiomeric excess and light-matter interactions for chiral semiconductors. *Sci. Adv.* **3**, e1601159 (2017).